



Steam reforming of methanol using Cu-ZnO catalysts supported on nanoparticle alumina

Samuel D. Jones, Luke M. Neal, Helena E. Hagelin-Weaver^{*}

Department of Chemical Engineering, University of Florida, Gainesville, FL 32611, United States

ARTICLE INFO

Article history:

Received 10 January 2008

Received in revised form 9 April 2008

Accepted 19 May 2008

Available online 5 June 2008

Keywords:

Methanol steam reforming

Cu/ZnO/Al₂O₃ catalysts

Hydrogen production

Nanoparticle alumina

CO selectivity

ABSTRACT

Methanol steam reforming was studied over several catalysts made by deposition of copper and zinc precursors onto nanoparticle alumina. The results were compared to those of a commercially available copper, zinc oxide and alumina catalyst. Temperature programmed reduction, BET surface area measurements, and N₂O decomposition were used to characterize the catalyst surfaces. XRD was used to study the bulk structure of the catalysts, and XPS was used to determine the chemical states of the surface species. The nanoparticle-supported catalysts achieved similar conversions as the commercial reference catalyst but at slightly higher temperatures. However, the nanoparticle-supported catalysts also exhibited a significantly lower CO selectivity at a given temperature and space time than the reference catalyst. Furthermore, the turnover frequencies of the nanoparticle-supported catalysts were higher than that of the commercial catalyst, which means that the activity of the surface copper is higher. It was determined that high alumina concentrations ultimately decrease catalytic activity as well as promote undesirable CH₂O formation. The lower catalytic activity may be due to strong Cu–Al₂O₃ interactions, which result in Cu species which are not easily reduced. Furthermore, the acidity of the alumina support appears to promote CH₂O formation, which at low Cu concentrations is not reformed to CO₂ and H₂. The CO levels present in this study are above what can be explained by the reverse water-gas-shift (WGS) reaction. While coking is not a significant deactivation pathway, migration of ZnO to the surface of the catalyst (or of Cu to the bulk of the catalyst) does explain the permanent loss of catalytic activity. Cu₂O is present on the spent nanoparticle catalysts and it is likely that the Cu⁺/Cu⁰ ratio is of importance both for the catalytic activity and the CO selectivity.

© 2008 Elsevier B.V. All rights reserved.

1. Introduction

The rising cost of fossil fuels, in addition to environmental considerations has made fuel cells the subject of intense research as an alternative to internal combustion engines run on petroleum-based fuels. Due to lower operating temperatures and the fact that fuel cells are run on sulfur free fuels, they do not have the sulfur oxide or nitrous oxide emissions that are of concern with internal combustion engines. The low operating temperatures of proton exchange (or polymer electrolyte) membrane (PEM) fuel cells also make them suitable power sources for automotive applications. However, storing the hydrogen fuel as a liquid or high pressure gas on board a motor vehicle is undesirable. Having a hydrogen source in liquid form that can supply hydrogen when needed is preferable. One method of great interest in recent years is hydrogen production from methanol via steam reforming over copper-based

catalysts. Methanol is the preferred fuel for the reforming process given that it has a high H:C ratio, can be reformed at reasonably low temperatures (200–300 °C) and produces low amounts of CO [1]. Low CO concentrations are important in fuel cell applications, as even CO concentrations on the order of a few ppm will poison the PEM fuel cell anode [2]. Consequently, not only are high yields of hydrogen at low temperatures important, a CO-free or nearly CO-free hydrogen must also be produced. This is a great challenge to the heterogeneous catalyst community.

The most common methanol steam reforming catalyst is Cu/ZnO/Al₂O₃ [3]. Zinc oxide is added to improve the dispersion of the Cu, increase the so-called “spill over” effect, increase the degree of micro-strain in the catalyst surface, and improve the reducibility of the CuO precursor [4–16]. The adsorption of methanol is generally thought to occur on the copper metal (or Cu₂O), and hydrogen atoms dissociate from the adsorbed methanol and move (“spill over”) from the copper onto the ZnO, where they are loosely bound [16]. High surface area alumina appears very useful in reducing the loss of copper surface area through sintering [5,7,9,10]. However, despite the common use of alumina as a support in these reactions,

^{*} Corresponding author. Tel.: +1 352 392 6585; fax: +1 352 392 9513.

E-mail address: hweaver@che.ufl.edu (H.E. Hagelin-Weaver).

it has been shown recently that the H_2 yield decreases with increasing alumina concentration and that Al_2O_3 actually hinders the reforming reaction [9].

Despite the large number of articles available in the literature on copper-based steam reforming catalysts, there is still some controversy on the actual reaction mechanism. Detailed mechanistic studies of copper and zinc oxide on alumina catalysts have been performed by Peppley et al. and they concluded that three reactions must be considered when methanol reacts with water over copper-based catalysts [4,17]. These include: steam reforming of methanol to form hydrogen and carbon dioxide (Eq. (1)); the water-gas-shift (WGS) reaction (Eq. (2)), and the decomposition of methanol (Eq. (3)).



The thermodynamic equilibrium of the steam reforming reaction (1) has been shown to be over 99.9% conversion of methanol above 500 K at 1 atm [18]. In agreement with the results from Peppley et al. [17], other authors have found that the methanol decomposition reaction occurs in parallel with the steam reforming reaction [19], particularly at low conversions [20]. In contrast, Agrell et al. reported that CO production was negligible at very short space times (low conversions) under the conditions used in their study [11]. Several groups have also reported that CO is a secondary product (formed from CO_2 via the reverse water-gas-shift reaction) rather than a primary product (formed via direct methanol decomposition) [7,11,12,21,22].

Another area which has received considerable attention in the literature is the nature of the active sites, in particular the oxidation state of the copper in the steam reforming catalysts. It is generally agreed that Cu^{2+} is inactive and Cu^+ as well as Cu^0 are active species in the steam reforming reaction [14,23–25]. While some authors do not attribute any activity to Cu^+ [26], other groups have found that stabilizing Cu_2O with “reducible” oxides, such as ZrO_2 and CeO_2 , results in highly active methanol reforming catalysts [14,23–25].

Catalyst characterizations of Cu-ZnO-based steam reforming catalysts have indicated the formation of spinel-type compounds, either CuAl_2O_4 or ZnAl_2O_4 [21,27–31]. Several groups have identified the spinel phase as CuAl_2O_4 [21,27,28,30], while other authors report that ZnAl_2O_4 forms in the bulk and that CuAl_2O_4 exists only as a surface species [28,29,31]. Formation of surface CuAl_2O_4 results in the presence of inactive Cu^{2+} species and is undesirable given that the total number of active Cu^0 or Cu^+ atoms is decreased. On the other hand, ZnAl_2O_4 has been found to be a very efficient catalyst support in the methanol steam reforming reaction [32]. Therefore, determination of the type of spinel phase formed is critical.

The above summary of previous results reveals the complexity of Cu-ZnO-based methanol steam reforming catalysts. These catalysts are further complicated by the fact that a high Cu surface area is not always a sufficient requirement for a high catalytic activity. Recent studies indicate that the catalytic activity can be improved by introducing micro-strain in the active metal phase [5,6,23]. Consequently, engineering catalysts at the nanometer scale to achieve higher catalytic activities is important in these reactions. It is our hypothesis that starting with nanoparticle alumina as the support, it is possible to prepare highly active Cu particles on the catalysts. Therefore, the goals of this study are to prepare catalysts using nanoparticle alumina supports and determine how they

compare with more traditionally prepared catalysts. The present study will focus on the following:

- (1) Investigate if Al_2O_3 is a retardant in the reforming reaction, or if it is possible to make high performance reforming catalysts with copper and zinc oxides deposited onto nanoparticle Al_2O_3 .
- (2) Determine if there are advantages to using nanoparticle precursor materials in catalyst synthesis.
- (3) Determine if CO is produced solely via the water-gas-shift, or if methanol decomposition also plays a role over the nanoparticle catalysts.
- (4) Determine if the surface and structural characteristics of the nanoparticle-supported catalysts differ from those reported in the literature and how they affect the catalytic activity.

2. Experimental

2.1. Catalyst preparation

Catalysts in this study are named according to the concentrations of the active metal oxides, promoter, and support as mass percentages. Labels are assigned according to the concentrations of CuO, ZnO, and Al_2O_3 , respectively, in the catalyst sample. For instance, the 35/35/30 sample is 35% CuO, 35% ZnO, and 30% Al_2O_3 by mass. The 35/35/30 and 42/47/11 catalysts were prepared via a sequential wet impregnation method with the goal of attaining 2.0 g of the finished catalyst sample. For these catalysts, a mass of commercial nanoparticle Al_2O_3 (NanoScale, surface area $\sim 650 \text{ m}^2/\text{g}$) was dispersed in deionized water. A solution of $\text{Zn}(\text{NO}_3)_2$ (Alfa Aesar) was then added to the mixture. The total volume of water used was 50 ml, which resulted in dispersions with nitrate concentrations of 0.18 M for the 35/35/30 and 0.21 M for the 42/47/11 samples. The water was boiled off until a paste consistency was formed. The pastes were dried overnight at 105 °C and calcined at 350 °C for 3 h. The resultant ZnO/ Al_2O_3 samples were ground and redispersed in water. The copper was then added as an aqueous solution $\text{Cu}(\text{NO}_3)_2$ (Alfa Aesar) to the dispersion (water added = 50 ml and the molar concentration of the copper nitrate precursor: 0.18 M copper nitrate for the 35/35/30 catalyst and 0.24 M for the 42/47/11 catalyst). The water was boiled off and the paste was dried in the same manner as in the previous step. The sample was then calcined a second time at 350 °C for 3 h.

For the sequentially precipitated 5/5/90 catalyst 1.8 g of the nanoparticle Al_2O_3 support was dispersed into 50 ml of deionized water and a solution of $\text{Zn}(\text{NO}_3)_2$ added, which resulted in a 0.025 M zinc nitrate dispersion as described above. The mixture was titrated with a 50% stoichiometric excess (i.e. 50 ml of 0.0375 M) solution of NaOH and then aged overnight before it was filtered and washed by stirring in deionized water again overnight. The catalyst dispersion mixture was filtered a second time and the resulting catalyst dried in an oven at 105 °C over night and calcined at 450 °C for 3 h. A calcination temperature of 450 °C was used instead of 350 °C for this catalyst since the lower calcination temperature resulted in higher CO selectivities. The lower calcination temperature would also give less reproducible results, in that the conversion and the selectivity would change with time on stream. The calcined 5/5/90 sample was then ground and again dispersed in water. The precipitation and calcination procedures were repeated exactly as described above with a solution of $\text{Cu}(\text{NO}_3)_2$.

The commercially available Süd-Chemie catalyst is approximately 42% CuO, 47% ZnO and 11% Al_2O_3 by mass according to the manufacturer. This catalyst was designed as a low temperature

shift catalyst, which is typical for commercially available reforming catalysts.

2.2. Reaction experiments

The catalyst powders were pressed into pellets in a 1/2 in. diameter pellet die under 2 tons of force exerted by a Carver press. For all reactor experiments in this study, the catalyst pellet of the sample to be loaded into the reactor was crushed and sieved to obtain particles with sizes between 500 μm and 1 mm for activity testing. Catalyst activity measurements were carried out in a stainless steel reactor with an inner diameter of 11.81 mm. Approximately 300 mg of catalyst was packed between two quartz wool plugs to keep the catalyst bed in place. Catalyst mass loading was held constant for all reactor experiments in this study. The reactor tube was then placed inside a horizontal Barnstead Type F2100 Tube Furnace. Depositing the catalyst over the quartz wool served to hold the catalyst bed in place and also to avoid channeling. Argon gas was used as both the carrier gas for the experiments and the internal standard for the gas chromatograph. Argon flow through the system is controlled using an MKS series M100B mass flow controller accurate to within 1% of the full scale reading (200 sccm). The temperature was measured with an Omega type K thermocouple at the effluent side of the packed bed. Methanol and water were introduced as a mixed liquid solution by a KDS model 100 syringe pump. The liquids travel a very short distance to an in-house built evaporator coil housed in a ceramic heater. The temperature of the heater is controlled by an Omega CN616 series PID controller which maintains the evaporator heater at a sufficient temperature to ensure single phase flow.

Lines on the system are constructed of stainless steel tubing and are wrapped in heating tapes to ensure that unreacted methanol and water do not condense in the process lines. For all catalyst experiments in this study, the water/methanol ratio was constant at 1.4 (v/v) (~ 3.1 mol/mol). After exiting the reactor, the unreacted condensable species are removed in an ice bath condenser and the remaining non-condensable species enter an on-line Agilent 6890 gas chromatograph. The gas chromatograph is equipped with both a thermal conductivity detector and a flame ionization detector in series and has two packed columns, a polar Porapak Q capillary column and a molecular sieve. The molecular sieve separates all permanent gases while the polar packed column separates all other components. The chromatograph was calibrated using known flow rates of pure gases (CO , CO_2 , H_2 and CH_4) with Ar as the internal standard (though no CH_4 was ever detected in the experiments). Effluent concentrations of all components are monitored by the thermal conductivity detector. To increase the sensitivity toward CO and CO_2 a methanizer is also used together with the flame ionization detector to monitor these species. CH_2O vapor calibration was performed using a saturation chamber, since the vapor pressure (and total system pressure) is known at a set temperature. Condensate analysis was performed via liquid injections into the same chromatograph. Calibrations for CH_2O in the condensate were performed using a saturated CH_2O solution (Fisher Scientific) and diluting it to known concentrations of CH_2O . All chromatography data is analyzed using the Cerity 3.0 software. Since methanol is not introduced into the chromatograph, conversion is calculated by performing a carbon balance. This assumes that unreacted methanol is the only carbon containing species not entering the chromatograph. However, in some cases CH_2O was formed in the reaction. In these cases, condensate analysis showed that even at the highest CH_2O production rates, the water in the condenser had either no CH_2O at all, or only negligible amounts of dissolved CH_2O . In either case the tiny amount of CH_2O in the condensate does not change the shape of

the conversion curves shown in this publication since the amount of CH_2O dissolved in the condensate is several orders of magnitude less than the amount of CO_2 produced in the reactor. Essentially all CH_2O in the system is present in the vapor phase. There is also no evidence of coking of the catalysts (see Section 3.5), which would further complicate calculating an accurate conversion. Catalyst samples were activated in situ in 10% H_2 in Ar (45 sccm total flow rate) at 300 $^\circ\text{C}$ for 3 h before being exposed to the reactant mixture.

Gas samples from the reactor were taken after the system had reached steady state, approximately 2 h after system start-up. The concentrations of CO, CO_2 and H_2 were measured as a function of temperature by starting at 200 $^\circ\text{C}$ and increasing the temperature in increments of approximately 15 $^\circ\text{C}$ for each data point. At least six gas samples were taken for each data point, and all data was seen to be reproducible. Points plotted in the figures are the averages of these samples. An average standard deviation of $\pm 6\%$ for the methanol conversion and $\pm 1\%$ for the CO selectivities were calculated for the reference catalyst. In cases when space time was the independent variable, the reactor feed was started at a low flow rate and the flow was gradually increased to examine decreasing space times. The curves were repeated by starting with a fresh sample and taking measurements at high flow rates and decreasing the flow to examine increasing space times. This procedure ensures that the curves are reproducible and that catalyst aging can be ruled out in the analysis. The catalyst behavior, even the sharp changes in activity, was verified by repeated experiments in each case using fresh catalysts. In all cases catalyst deactivation due to time on stream for relevant time lengths (~ 40 h) was not found to affect the analysis or conclusions in this study.

The calculated CO selectivity (S_{CO}) is defined as the percentage of the CO produced relative to the sum of CO plus CO_2 produced (Eq. (4)).

$$S_{\text{CO}} [\%] = \frac{p^{\text{CO}}}{p^{\text{CO}} + p^{\text{CO}_2}} \times 100 \quad (4)$$

where $p^{\text{CO}x}$ is the partial pressure or molar concentration of CO or CO_2 .

After a completed reaction, the catalysts were cooled to room temperature under an argon atmosphere and loaded into a sample vial where the air was replaced with argon. The samples were then taken to the XPS and XRD instruments for further analysis.

2.3. BET surface area analysis

Brunauer–Emmett–Teller (BET) surface area measurements were performed on a Quantachrome NOVA 1200 instrument. Samples were outgassed under vacuum for 3 h at room temperature for fresh catalysts and at 105 $^\circ\text{C}$ for spent catalysts. The BET was performed over five isotherms, which gave roughly linear fits.

2.4. Temperature programmed reduction experiments

Temperature programmed reduction (TPR) measurements were performed in a Quantachrome ChemBET 3000 instrument. For TPR measurements, 55 mg of the catalyst was loaded in a quartz tube reactor and secured with plugs of quartz wool on both ends. An Omega K-type thermocouple monitored the temperature in the catalyst bed. Reduction was carried out at a heating rate of 5 $^\circ\text{C}$ per minute up to a temperature of 500 $^\circ\text{C}$ under a flow of 5% H_2/N_2 mixture at a total flow rate of 70 sccm until the catalyst was fully reduced and did not consume additional hydrogen. The hydrogen uptake was continuously monitored using a TCD detector during the reduction.

2.5. N₂O decomposition experiments

The copper surface areas were also measured on the ChemBET 3000 instrument (QuantaChrome Corporation) using the N₂O decomposition method, as is typically done for copper-based reforming catalysts [7,23,33,34]. The catalysts were loaded in a quartz tube reactor and held in place by quartz wool. Prior to each measurement the samples were reduced in pure H₂ at 300 °C (20 sccm) and then cooled overnight to room temperature under helium. During the measurements helium gas flowed over the samples at a rate of 70 sccm, and the reactive adsorption of N₂O was performed by titrating known amounts of N₂O over the catalyst surface and monitoring the N₂ evolved using a thermal conductivity detector. With this instrument unreacted N₂O is removed from the system through use of a liquid argon cold trap, which condenses out N₂O but allows N₂ to pass onto the TCD. In this way N₂O is titrated over the sample until no signal is recorded on the TCD. At this point the surface is saturated and no further N₂O reacts to N₂. The total amount of N₂ formed (or N₂O consumed) was determined and used to calculate the amount of copper surface atoms according to the stoichiometry in Eq. (5).



The copper surface area was calculated from these results assuming a copper surface density of 1.47×10^{19} copper atoms per square meter [23,33]. The dispersion is defined as the ratio of copper atoms on the surface of the catalysts to the total number of copper atoms in the catalyst. The error in this measurement has been estimated by other researchers to be approximately 15%, which is reasonable in the current investigation as well [23].

2.6. Catalyst density measurements

For the calculations of space time (volumetric flow rate divided by the volume of catalyst), the catalyst densities were measured on a Quantachrome Ultrapyc 1000 Gas Pycnometer.

2.7. X-ray diffraction analysis

The XRD data was gathered on a Philips powder X-ray diffractometer using Bragg–Brentano geometry with Cu K α radiation ($\lambda = 1.54 \text{ \AA}$). The XRD spectrum was recorded in a 2θ range of 20–80° at ambient conditions. Diffraction patterns were obtained for all samples after calcinations and for selected samples after reductive pretreatment and after reaction. Average particle sizes were calculated from the line-broadening of the XRD peaks using the Sherrer equation [Eq. (6)].

$$d = \frac{K \cdot \lambda}{(\text{FW} \cdot \cos(\theta))} \quad (6)$$

In this equation K is a constant generally taken as unity, λ is the wavelength of the incident radiation, FW is the full width at half max and θ is the peak position.

2.8. X-ray photoelectron spectroscopy analysis

The XPS data was collected using a Kratos XSAM 800 XPS instrument equipped with a hemispherical analyzer. The samples were supported on double-sided tape during the measurement. Incident radiation was from an aluminum anode with $h\nu = 1486.6 \text{ eV}$. The pass energy settings on the instrument were set to “low” for the survey spectra and “medium” for the scans of the individual element peaks. Pressure was maintained at 10^{-7} Torr or less during the entire measurement. Charge shift corrections

were made by assuming a C 1s signal of 284.5 eV. The data collected from this instrument using the C 1s as the shift reference resulted in binding energies 2 eV above what is expected for the Cu 2p peaks. To test if the observed high binding energies were due to differential charging, i.e. different sections of the XPS spectrum experience a different charge, the fresh 35/35/30 catalyst was selected for analysis using a different XPS instrument. In the second system, the catalysts are pressed into an aluminum cup before entry into the UHV chamber [35]. The binding energies for the Cu 2p peaks obtained from the fresh 35/35/30 catalyst in this system is centered at 933.6 eV as expected for CuO, which is also in agreement with the XRD data and the conclusions from the XPS data obtained from the other system. Consequently, the XPS peaks, such as the Cu 2p peaks, obtained from the 35/35/30 catalyst using the Kratos system were shifted to match the binding energies obtained from the same catalyst in the second system. The shift difference was then used to adjust the peak positions from the other catalysts (5/5/90 and 42/47/11) in this study. The atomic percentages of each element on the surface were calculated from the areas under the peaks taking into consideration the atomic sensitivity factor for each element and specified peak.

3. Results and discussion

3.1. Catalytic activity and selectivity measurements

3.1.1. Methanol conversion

Fig. 1 shows methanol conversion as a function of temperature at constant liquid feed flow rate (0.80 ml/h) for each catalyst tested. It is evident from the conversion plot that the reference catalyst is more active at a lower temperature than any of the nanoparticle-supported catalysts, although the activities of the reference and the 42/47/11 catalysts are fairly similar below 280 °C. It is also evident that no catalyst is even close to approaching the equilibrium conversion (>99%) under these conditions (see Fig. 1). However, at higher temperatures, both the reference catalyst and the 42/47/11 catalyst lose activity very rapidly. The 42/47/11 catalyst exhibits severe deactivation at

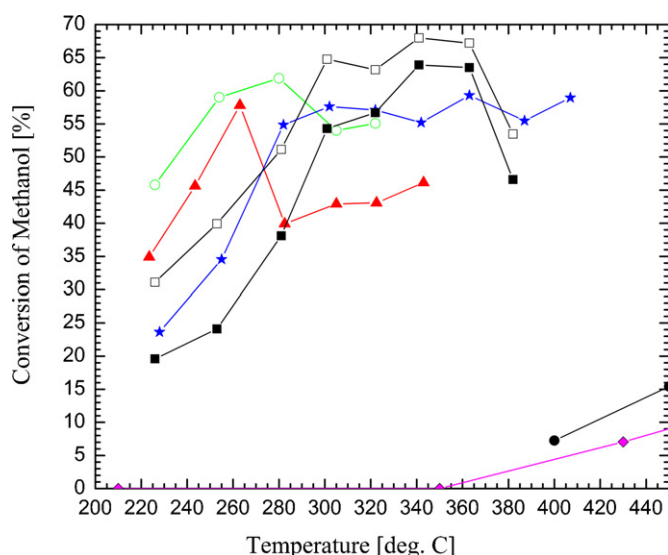


Fig. 1. Conversion of methanol as a function of temperature at constant liquid feed flow rate (0.8 ml/h). (—□—) catalyst 5/5/90 total conversion, (—■—) catalyst 5/5/90 conversion to CO and CO₂, (—★—) catalyst 35/35/30, (—▲—) catalyst 42/47/11, (—○—) reference catalyst, (—◇—) blank run (no catalyst or support) and (—●—) conversion to CO and CO₂ over nanoparticle alumina.

only 280 °C. The reference catalyst does not exhibit significant deactivation until 20 °C higher. No reaction data for the reference catalyst could be obtained above approximately 320 °C due to severe deactivation. Significant deactivation of the 5/5/90 catalyst does not occur until over 400 °C, whereas significant loss of activity for the 35/35/30 catalyst did not occur in the temperature range investigated in this study. The deactivation of the catalysts is irreversible. After a second reduction in dilute H₂ none of the deactivated catalysts could be returned to their original activity levels. The fact that no catalyst achieved over 65% conversion at the space time used in Fig. 1 regardless of temperature reflects a kinetic limitation (since the equilibrium conversion of the methanol steam reforming reaction is 99% or higher in this temperature range). Higher conversions can be achieved with these catalysts by increasing the space time of the reactants, which is discussed in the next paragraph. Two curves are displayed for the 5/5/90 sample to differentiate between total CH₃OH reacted to all products (CO₂, CO and CH₂O), and CH₃OH reacted specifically to CO₂ and CO. No CH₂O was produced by any other catalyst.

Methanol conversion as a function of space time at 280 °C is presented in Fig. 2. The curves for the nanoparticle-supported catalysts in Fig. 2 show the classic sigmoidal growth shape asymptotically approaching a conversion of 100% at the highest space times. It is interesting to note that the curve for the reference catalyst does not display this shape, but rather goes through a very sharp change in the shape of the curve about halfway through the range of space times investigated. It is not evident what is responsible for the differences between the shapes of these curves. Purnama has also noted a “change in controlling kinetics at conversions higher than 70%” in his space time study of a commercially available Cu/ZnO/Al₂O₃ catalyst at 250 °C [12]. In the present experiment the distinct change in kinetics appears to occur at conversions of approximately 60%, but the jump in the curve does suggest a change in reaction mechanism. Conversions above 90% can be achieved rather easily at moderate temperatures for the 35/35/30 catalyst as well as the reference catalyst given sufficiently long space times. High conversions are also evident for the 5/5/90 sample, but a large amount of undesired CH₂O is produced by this catalyst with increasing space time. The other disadvantage with increasing the temperature or the space time is that the CO selectivity increases dramatically for all catalysts (see Figs. 3 and 4).

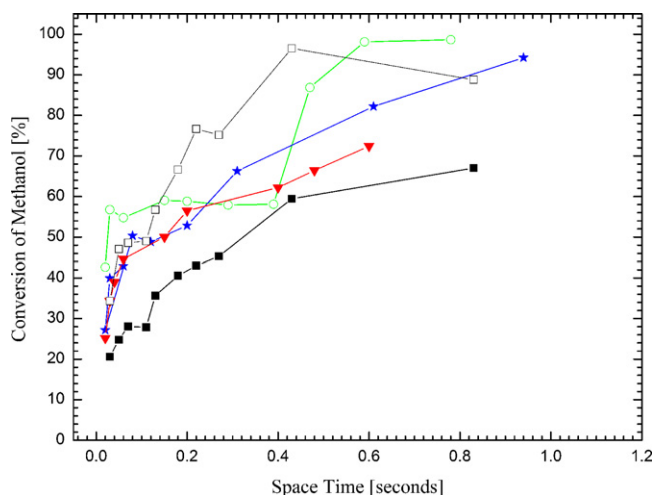


Fig. 2. Conversion of methanol as a function of space time, $T = 283$ °C. (—□—) catalyst 5/5/90 total conversion, (—■—) catalyst 5/5/90 conversion to CO and CO₂, (—★—) catalyst 35/35/30, (—▼—) catalyst 42/47/11, and (—○—) reference catalyst.

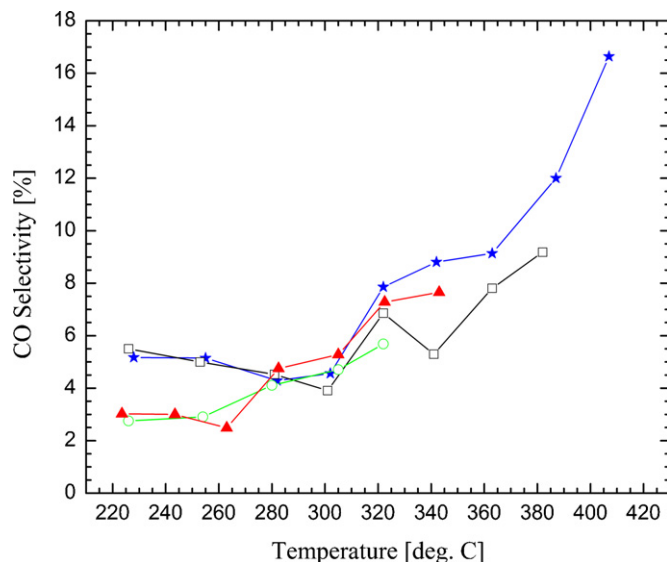


Fig. 3. CO selectivity, CO/(CO₂ + CO) as a function of temperature at constant liquid feed flow rate (0.8 ml/h). (—□—) catalyst 5/5/90, (—★—) catalyst 35/35/30, (—▲—) catalyst 42/47/11, (—○—) reference catalyst.

3.1.2. CO selectivity

Fig. 3 shows the CO selectivity as a function of temperature (liquid feed flow rate = 0.80 ml/h). Perhaps the most interesting feature of this figure is that the CO selectivity for the nanoparticle-supported catalysts actually decreases with increasing temperature up to approximately 300 °C (up to 260 °C for the 42/47/11 catalyst). In this temperature range (220–300 °C) the conversion is increasing rapidly with temperature for all catalysts (Fig. 1). The decrease in CO selectivity with increasing temperature is unexpected given that both CO production routes (the methanol decomposition reaction and reverse water-gas-shift reaction) are endothermic, which means that CO formation via these routes are favored both kinetically and thermodynamically with increasing temperature. However, the steam reforming reaction is also endothermic and the equilibrium conversion very high in this

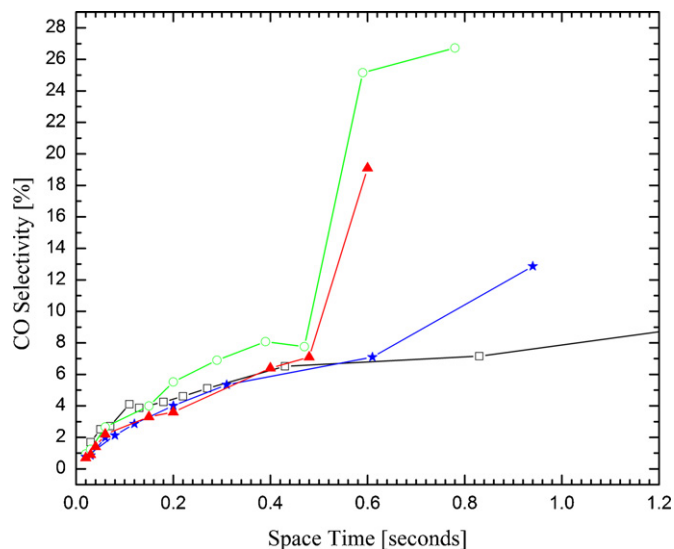


Fig. 4. CO selectivity, CO/(CO₂ + CO) as a function of space time at $T = 283$ °C. (—□—) catalyst 5/5/90, (—★—) catalyst 35/35/30, (—▲—) catalyst 42/47/11, (—○—) reference catalyst.

Table 1

Comparison of CO selectivity values at 50% and maximum conversion and fixed liquid feed flow rate, and CO selectivity at 65% conversion and 280 °C and variable space times (liquid feed flow rates)

Catalyst	Conversion [%]	Selectivity [%] ^a	Temperature [°C]	ST [s] ^b
5/5/90	50	3.9	300	0.21
35/35/30	50	4.3	280	0.13
42/47/11	50	2.5	255	0.14
Commercial	50	2.8	230	0.16
5/5/90	65 (max)	7	341	0.19
35/35/30	60 (max)	4.6	300	0.13
42/47/11	58 (max)	2.5	263	0.14
Commercial	62 (max)	4.1	280	0.15
5/5/90	65	6.5	280	0.40
35/35/30	65	5.3	280	0.31
42/47/11	65	6.4	280	0.40
Commercial	65	8	280	0.39

^a CO selectivity defined as in Eq. (4).

^b Space time.

temperature range. The fact that the CO selectivity decreases over this temperature range for all of the nanoparticle catalysts reveals that the rate of CO₂ formation is increasing more rapidly with increasing temperature than the rate of CO formation. Evidently, this is true for all nanoparticle catalysts, despite the significant differences in conversion in this temperature range. This may indicate that the catalyst surface is being altered at these temperatures, for example the Cu⁺/Cu⁰ ratio could be changing (see discussion in Section 3.5). Since the conversion and the CO selectivity are both very dependent on the temperature, it is useful to compare the CO selectivities of different catalysts at a specific conversion, as well as at the maximum conversion (Table 1). At 50% conversion the commercial catalyst and the 42/47/11 catalyst exhibit similar CO selectivities, which are considerably lower than those of the other nanoparticle-supported catalysts. More importantly, both the CO selectivity and the temperature at maximum conversion for the 42/47/11 catalyst are lower than the corresponding values for the commercial catalyst. Even though the maximum conversion is slightly lower for the 42/47/11 catalyst compared with the commercial catalyst, the decreased CO selectivity at 50% conversion indicates that the catalysts in this study can be tuned to outperform the commercial catalyst. This is further demonstrated by altering the space times, as shown below.

The CO selectivity as a function of space time at 280 °C is shown in Fig. 4. A temperature of 280 °C was selected since this temperature corresponds to the maximum conversion of the reference catalyst at a space time of 0.15 s. The figure shows that increasing the space time to the level needed for maximum conversion drastically increases the CO selectivity for all catalysts. Evidently, the reference catalyst has a higher CO selectivity at all space times than either the 35/35/30 or the 42/47/11 catalysts at this temperature. Only the 5/5/90 catalyst exhibits a slightly higher CO selectivity than the reference catalyst at space times below 0.15 s. The CO selectivities of both the reference catalyst and the 42/47/11 catalyst also display a large increase at space times around 0.5 s. The same discontinuous increase in conversion was evident for the reference catalyst in Fig. 2. Repeated tests verified that this step increase was neither due to catalyst aging nor an experimental artifact. The discontinuous change in conversion indicates a change in mechanism or reaction pathway for this catalyst at this specific value of the space time. The nanoparticle-supported catalysts show superior performance over the reference catalyst at high space times in that they can achieve increased methanol conversions without undergoing the jump in CO

selectivity that is evident in the reference catalyst. In fact at a conversion of 65% ($T = 280$ °C), the CO selectivity of all catalysts in this study are below that of the commercial catalyst (Table 1). The CO selectivity curves clearly display a zero intercept with decreasing space time. This has been taken as an indication that CO is a secondary product in several articles [11,12].

3.1.3. “Blank” experiments

The 5/5/90 catalyst produced CH₂O during the reforming reaction. No other catalyst showed detectable levels of CH₂O at any temperature. The fact that CH₂O is produced over the nanoparticle catalyst that contained 90% Al₂O₃ but not over the 30% or 11% Al₂O₃ catalysts suggests that the formation of CH₂O is a consequence of the high Al₂O₃ concentration. This was confirmed by performing a steam reforming experiment over bare nanoparticle alumina. The nanoparticle alumina produced relatively high levels of CH₂O, but the levels of CO and CO₂ were similar to those observed for the homogeneous reaction, i.e. a “blank” steam reforming experiment with no support or catalyst in the reactor (see Fig. 1). Furthermore, the CH₂O produced over the nanoparticle alumina was higher than over the 5/5/90 catalyst, which is likely an effect of a lower alumina surface area on the 5/5/90 catalyst due to coverage of the alumina by copper and zinc oxide. These results indicate that Al₂O₃ is active in CH₂O production, but not in reactions (1)–(3). Other researchers have also reported formation of CH₂O from CH₃OH on SiO₂/Al₂O₃ supports [36].

Of the catalysts in this study, the 35/35/30 catalyst demonstrated the greatest thermal stability. The 35/35/30 catalyst is more stable and does not suffer from the same degree of deactivation with temperature as the commercial reference and the 42/47/11 catalysts. The low CO selectivity coupled with the high durability of the catalyst means that high CH₃OH conversions can be achieved while generating lower amounts of CO than would be possible with a commercially available catalyst.

3.2. Surface area quantification

The BET surface areas before and after reaction, active copper surface areas, and turnover frequencies of the catalysts in this study are shown in Table 2. Evidently, the samples higher in alumina have a larger surface area. The nanoparticle-supported catalysts rely almost entirely on the Al₂O₃ for the surface area of the catalyst. Therefore, when the concentration of Al₂O₃ is small in the sample, the surface area is relatively low. The reference catalyst has a larger surface area compared with the nanoparticle-supported catalyst of the same composition. For the 5/5/90 and 35/35/30 nanoparticle-supported catalysts the surface areas of the spent catalysts are notably lower than those of the fresh catalyst samples. It is interesting to note that as the copper and zinc content increases the difference in surface area before and after exposure to the reaction conditions decreases. The surface area for the 42/47/11 catalyst is nearly unaffected by the reaction.

The decrease in surface area of the 5/5/90 catalysts after exposure to reaction conditions most likely corresponds to a sintering effect that causes some of the pores in the alumina support to be clogged due to particle growth of the copper. The loss of surface area is not due to the sintering of the alumina itself, given that there is no significant change in the Al₂O₃ particle size on this sample before and after the reaction (see Section 3.3, below). In contrast, on the reference catalyst, it appears that there is a slight increase in surface area after reaction. This effect was unique to the reference catalyst. Despite the fact that the reference catalyst did not lose surface area during the reaction, there was strong deactivation of this sample at elevated

Table 2
Surface characteristics of reforming catalysts

Catalyst	Nominal CuO concentration [wt%]	Cu surface area [m ² /g Cu]	Dispersion [%]	Fresh BET surface area [m ² /g]	Spent BET surface area [m ² /g]	Density [g/cm ³]	TOF at 280 °C [10 ³ s ^{−1}] ^a
Reference	42	20.2	3.1	68	82	5.2	34.6
42/47/11	42	3.5	0.5	23	24	5.8	160.1
35/35/30	35	5.3	0.8	46	40	5.0	128.8
5/5/90	5	56.2	8.6	218	170	3.5	59.4

^a TOF: turnover frequency, defined as the molecules of hydrogen produced per surface copper atom per second.

temperatures. Consequently, there is no correlation between the overall surface area and the catalytic activity for these catalysts.

The results of the N₂O titrations data provide a quantitative view of the differences in the surface copper concentration of the catalysts. Table 2 clearly shows that very high copper surface areas can be attained by using a high concentration of nanoparticle Al₂O₃. The copper surface area per gram of copper on the 5/5/90 sample is an order of magnitude higher than on the other nanoparticle catalysts, and more than double that of the reference catalyst. In comparing the data in Table 2 to the curves in Fig. 1, another interesting trend is evident. Despite the fact that the copper surface area per gram of the 42/47/11 is a fraction of that in the reference catalysts, the two samples achieve similar maximum conversions. The difference is that the turnover frequency of the 42/47/11 catalyst is dramatically higher than that of the reference sample. In fact, all nanoparticle-supported catalysts have higher turnover frequencies than the reference catalyst. The surface copper of the nanoparticle catalysts is clearly more active than the copper on the surface of the reference catalyst. However, the activity does not correlate with the Cu surface area of the catalysts. In fact, the turnover frequency (TOF) appears to correlate with the nominal CuO concentration rather than the Cu surface area for the nanoparticle catalysts. Alternatively, it can be stated that the TOF decreases linearly with increasing Al₂O₃ content (Table 2). The highest Al₂O₃ concentration (and highest copper surface area) is the 5/5/90 catalyst, which also displays the lowest turnover frequency. The catalyst with the lowest Al₂O₃ concentration (42/47/11) has the highest turnover frequency. Past researchers using copper-based methanol reforming catalysts have also noted that “properties other than copper surface area” affect the catalytic activity [7]. Obviously this is the case in the present study as well. It has been proposed that favorable morphology [37], increased reducibility [34], or simply higher “quality” [7] of the copper species in methanol reforming catalysts increases catalytic activity. In the samples used in this study, it is evident that increasing the alumina content of the samples tends to make the surfaces both less reducible and less active in the reforming reaction. This could be due to strong Cu–Al₂O₃ interactions at high Al₂O₃ concentrations, which in turn can alter the electronic properties of the Cu on the surface and also influence the Cu⁺/Cu⁰ ratios on the catalyst surfaces (see below). Hence, the “quality” of the copper decreases with increasing Al₂O₃ content despite the increase in Cu surface area, and high Al₂O₃ concentrations ultimately result in a less active catalyst.

3.3. XRD analysis

XRD spectra obtained from the fresh catalysts are shown in Fig. 5. The characteristic peaks of CuO are evident in all the spectra obtained from the fresh catalyst samples and a crystalline ZnO phase is present on the 35/35/30 and 42/47/11 catalysts, but not on the 5/5/90 catalyst. On the 5/5/90 the ZnO is below the detection limit or is present in amorphous form. No peaks due to alumina can be detected in the XRD spectrum obtained from the 35/35/30 or 42/47/11 catalysts. This is not surprising due to the low crystal-

linity and the lower alumina concentration of the catalysts compared to the 5/5/90 catalyst. There are small broad peaks visible in the spectrum of the 35/35/30 catalyst at $2\theta = 31.3^\circ$, 37.1° , 44.6° , 55.6° , 59.2° , and 65.1° which are not due to CuO or ZnO. The 2θ values of the peaks are consistent with those obtained from aluminate species such as CuAl₂O₄ [38] or ZnAl₂O₄ [39]. Since both the CuAl₂O₄ and ZnAl₂O₄ have nearly identical diffraction patterns it is difficult to distinguish between the two in the XRD spectrum obtained from the 35/35/30 catalyst [29,38,39]. An experiment was therefore designed to determine the type of aluminate formed during the catalyst preparation procedures used in our study. Two sample catalysts composed of ZnO/Al₂O₃ and CuO–Al₂O₃ were prepared using the catalyst preparation method described above, keeping the CuO:Al₂O₃ and ZnO:Al₂O₃ ratio the same as in the 35/35/30 catalyst (i.e. at 1.17 by mass), and characterized with XRD measurements. The presence of an aluminate phase was visible with XRD only in the ZnO–Al₂O₃ sample (not shown). This result suggests that the aluminate phase seen in the XRD spectra obtained from the 35/35/30 catalysts is ZnAl₂O₄ and not CuAl₂O₄ as has been assigned in the past [21]. However, due to the presence of copper in addition to zinc on these catalysts, the presence of CuAl₂O₄ cannot be ruled out completely. Our assignment of a ZnAl₂O₄ phase agrees with the assignment made by Turco et al. [31] in a related study.

Table 3 shows average crystal sizes of all species visible in the XRD spectra calculated using the Sherrer equation [Eq. (6)]. The sizes of the CuO particles are slightly smaller on catalyst 42/47/11 (27 nm) compared with catalyst 35/35/30 (34 nm), despite the higher CuO concentration of the 42/47/11 catalyst. This contradicts the lower dispersion observed on the 42/47/11 catalyst (smaller particle sizes give larger surface areas and higher dispersions), and is likely due to more ZnO covering the CuO on catalyst 42/47/11

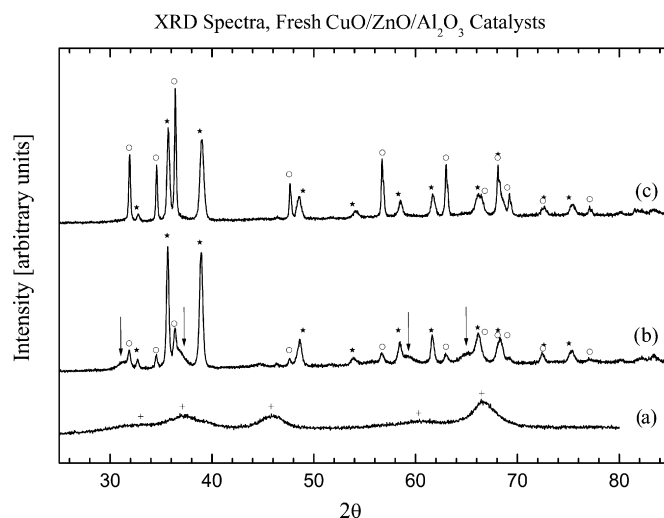


Fig. 5. XRD spectra obtained from fresh catalysts: (a) 5/5/90 CuO/ZnO/Al₂O₃ catalyst, (b) 35/35/30 CuO/ZnO/Al₂O₃ catalyst and (c) 42/47/11 CuO/ZnO/Al₂O₃ catalyst. (+) γ -Al₂O₃, (★) CuO, (o) ZnO. Arrows indicate peaks due to ZnAl₂O₄.

Table 3

Particle sizes of the different compounds on the various CuO/ZnO/Al₂O₃ and Cu/ZnO/Al₂O₃ catalyst in the current work

Particle sizes [nm]						
Catalyst	Species					
	Cu	CuO	ZnO	ZnAl ₂ O ₄	Cu ₂ O	Al ₂ O ₃
5/5/90 CuO/ZnO/Al ₂ O ₃ Fresh	–	13.8	–	–	–	4.5
5/5/90 Cu/ZnO/Al ₂ O ₃ Spent	–	–	–	–	7.3	4.7
35/35/30 CuO/ZnO/Al ₂ O ₃ Fresh	–	33.6	32.1	7.8	–	–
35/35/30 Cu/ZnO/Al ₂ O ₃ Spent	35	–	33.4	6.9	–	–
42/47/11 CuO/ZnO/Al ₂ O ₃ Fresh	–	26.9	57.5	–	–	–
42/47/11 Cu/ZnO/Al ₂ O ₃ Spent	22.5	–	34.7	–	–	–

The particle sizes have been determined from the XRD data using the Sherrer equation.

compared with catalyst 35/35/30. This may be expected due to the higher ZnO content on catalyst 42/47/11 and the ZnO particle sizes are also considerably larger on catalyst 42/47/11 (58 nm) compared with those on catalyst 35/35/30 (32 nm). It is interesting to note that no CuAl₂O₄ or ZnAl₂O₄ can be detected on the 42/47/11 catalyst. Consequently, if present, the aluminates are either amorphous or below the detection limit of the XRD instrument. Another interesting observation is that the particle sizes of the aluminate species are smaller than for the CuO and ZnO species. The Sherrer equation gives a value of 8 nm for the aluminate. The same behavior of the aluminate phase was observed in the study by Murcia-Mascarós et al. [21]. The small particle size observed is likely due to the strong metal–support interactions that result in formation of this compound.

After reduction treatment and exposure to the reaction conditions no crystalline CuO is present on any of the catalysts (Fig. 6A and B). The XRD spectra obtained from all catalysts exhibit features due to Cu metal after these treatments. In fact, the spectra obtained from the 35/35/30 and 42/47/11 catalysts after reductive treatment (not shown) are indistinguishable from those obtained after exposure to the reactions conditions. In addition to the peaks due to Cu metal, the XRD spectrum obtained from the spent 5/5/90 catalyst also exhibits peaks located at $2\theta = 36.8^\circ$, 42.5° , 61.7° and 73.9° . These peak positions are consistent with Cu₂O [40]. The fact that the Cu₂O species can be detected with XRD is remarkable, since Cu₂O has only been detected previously using XRD on catalysts with significantly higher copper contents [24,41]. Furthermore, in those cases it appears that the ZrO₂ used as the support stabilizes the Cu₂O [24,41], and such support stabilization of Cu₂O is unlikely on Al₂O₃. Fig. 6B shows that only Cu metal is present on the 5/5/90 catalyst after the reductive treatment. This unequivocally demonstrates that the Cu₂O is formed during the reforming reaction and is not a result of either the brief air exposure before analysis or incomplete reduction during the pretreatment. To our knowledge, Cu₂O has never been observed on Al₂O₃-supported spent reforming catalysts. This result also indicates that increasing the concentration of nanoparticle Al₂O₃ alters the redox properties of the surface (as indicated above), which in turn affects the surface activity. The Al₂O₃ makes the surface more difficult to reduce (see below), which apparently translates to a decrease in turnover frequency, as seen in the previous section.

The reduction treatment and exposure to the reaction conditions does not appear to affect the Al₂O₃ particle size on the 5/5/90 catalyst (see Table 3). The particle sizes of the Cu metal on the spent 35/35/30 catalyst are similar to those of the CuO particles on the fresh catalyst (~33 nm). This suggests that there is some sintering of the copper during the reduction (or reaction) [i.e. there are more Cu atoms per particle after reduction and reaction]. On catalyst 42/47/11 the Cu metal particles are slightly smaller

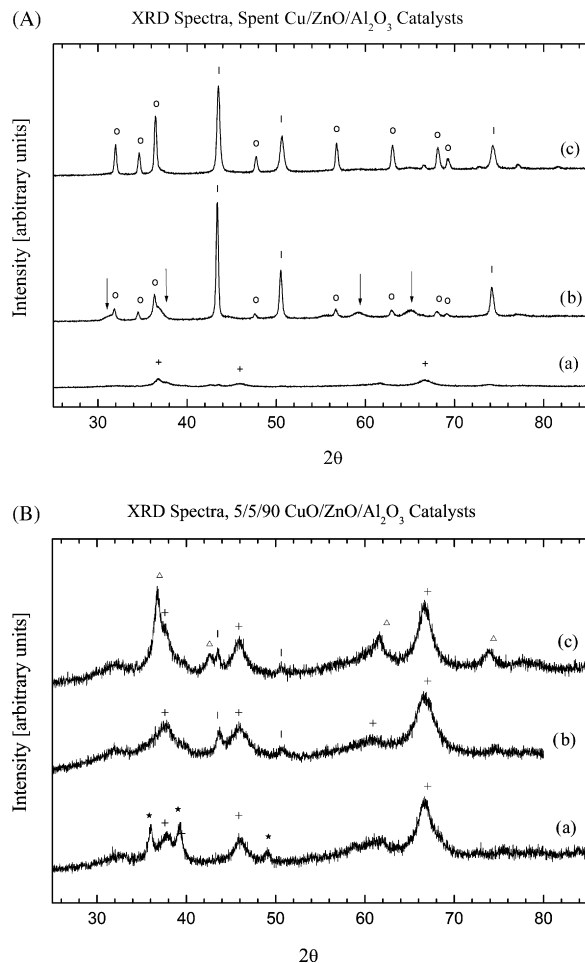


Fig. 6. XRD spectra obtained from A: (a) spent 5/5/90 Cu/ZnO/Al₂O₃ catalyst, (b) spent 35/35/30 Cu/ZnO/Al₂O₃ catalyst, and (c) spent 42/47/11 Cu/ZnO/Al₂O₃ catalyst. B: (a) fresh 5/5/90 CuO/ZnO/Al₂O₃ catalyst, (b) reduced 5/5/90 CuO/ZnO/Al₂O₃ catalyst, and (c) spent 5/5/90 CuO/ZnO/Al₂O₃ catalyst. (+): γ -Al₂O₃, (★): CuO, (○): ZnO, (|): Cu metal and (Δ): Cu₂O.

(23 nm) than the CuO particles on the fresh catalyst (27 nm). Although some sintering is expected, this indicates that the sintering of copper is more severe on the 35/35/30 catalyst compared with the 42/47/11 catalyst. The ZnO appears to be unaltered after reduction and reaction on the 35/35/30 catalyst, while on the 42/47/11 catalyst they appear to be smaller after reduction and reaction (35 nm) compared to the fresh 42/47/11 catalyst (58 nm). The particle size of ZnAl₂O₄ on the 35/35/30 catalyst is not altered significantly, as expected. Other research groups have also noted that aluminates can be very difficult to reduce [27,30,42]. Even at elevated temperatures and under vacuum, a CuAl₂O₄ spinel phase is fairly stable and will not readily reduce to Cu and Al₂O₃ [42]. Hence, it is not surprising that under the reduction treatment and the reaction conditions of these experiments the ZnAl₂O₄ spinel phase is also rather stable.

Despite the fact that sintering of the Cu metal appears to be the highest on the 35/35/30 sample, this catalyst did not deactivate as rapidly as the 42/47/11 catalyst. Therefore, the catalyst deactivation in the activity measurements is not simply due to sintering of copper in the samples (see Section 3.5).

3.4. Temperature programmed reduction measurements

TPR experiments provide further insight into these catalysts. Previous results indicate that the catalytic activity correlates with

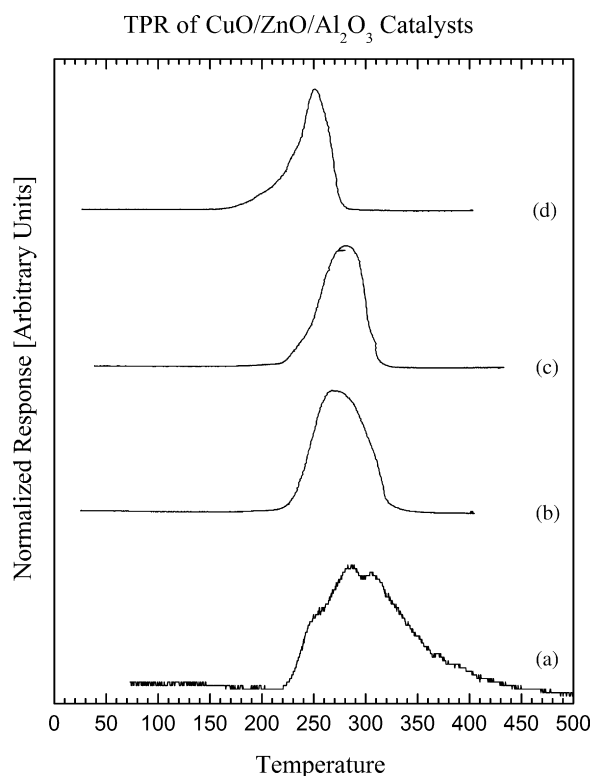


Fig. 7. Normalized temperature programmed reduction (TPR) profiles. (a) 5/5/90, (b) 35/35/30, (c) 42/47/11, and (d) reference catalysts.

the reducibility of the copper species on the surface [34]. If this is true, then the commercial catalyst would be the easiest to reduce and the 5/5/90 the most difficult, which is indeed the case. The commercial catalyst starts to reduce below 200 °C, which is 30 °C lower than the nanoparticle catalysts (Fig. 7). While reduction of the 5/5/90 catalyst starts at the same temperature as the other nanoparticle catalysts (i.e. 230 °C), hydrogen consumption does not end until well above 400 °C, long after the other catalysts are fully reduced. The high reduction temperature of the 5/5/90 catalyst is likely a result of the smaller copper particle size on this catalyst (14 nm versus 34 nm and 27 nm for the 35/35/30 and 42/47/11 catalysts, respectively) and stronger copper–alumina interactions. It has been previously reported that “reduction occurs at higher temperatures, or more reluctantly, as CuO particle size decreases” [43]. The TPR profiles of the 35/35/30 and 42/47/11 catalysts are similar, with reduction beginning at approximately 225 °C and ending around 320 °C. However, two differences can be observed; (1) the hydrogen consumption of the 35/35/30 catalyst peaks at approximately 265 °C, while that of the 42/47/11 catalyst does not reach a maximum until 15 °C higher and (2) the reduction for the 35/35/30 catalyst is not completed until 15–20 °C higher than that for the 42/47/11 catalyst. Consequently, at high alumina concentrations, the CuO precursor on the nanoparticle catalysts is more difficult to reduce and this results in a less active catalyst, i.e. the TOF is higher for lower Al₂O₃ concentrations. The observed correlation between catalytic activity (turnover frequency) and ease of CuO reduction on the catalysts is consistent with the literature [44].

3.5. XPS analysis

XPS measurements were performed to determine how the surface composition and the valence state of the surface copper vary between the different catalysts and between the fresh and spent catalysts. Part of the goal with these measurements is to

Table 4

Relative surface concentrations of different elements calculated from the atomic concentrations at the surface

Ratio [at.%]	Catalyst					
	5/5/90		35/35/30		42/47/11	
	Fresh	Spent	Fresh	Spent	Fresh	Spent
Zn 2p/Cu 2p	0.6	1.9	2.5	3.0	3.3	3.9
C 1s/Al 2p	1.0	1.0	1.2	1.2	1.2	1.1
Cu 2p/Al 2p	0.4	0.1	0.4	0.5	0.4	0.4
Zn 2p/Al 2p	0.2	0.3	1.0	1.4	1.2	1.7

The atomic concentrations are based on the peak areas of the peaks listed in the table with adjustments made for the sensitivity factors of each peak.

determine if Cu₂O can be detected on the catalysts after exposure to the reaction conditions.

3.5.1. Fresh catalysts

The XPS survey spectra reveal that despite the higher CuO content, the Cu peaks obtained from the 42/47/11 catalyst have lower intensities compared to those obtained from the 35/35/30 catalyst, while the peaks due to ZnO are more intense. This is evident as a higher Zn/Cu ratio on catalyst 42/47/11 (Table 4). Consequently, a higher fraction of CuO on the 42/47/11 catalyst is covered with ZnO compared with the 35/35/30 catalyst, which is in agreement with the conclusions from the XRD particle sizes and the Cu surface areas.

The Cu 2p peaks obtained from the fresh and spent catalysts are shown in Fig. 8. The presence of a Cu²⁺ species on the fresh catalysts is evident from the intense satellite peak at a binding

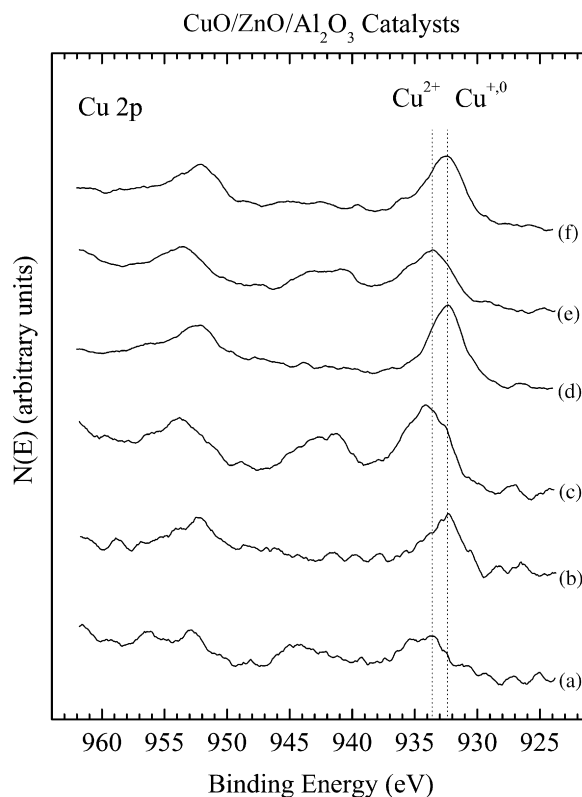


Fig. 8. XPS spectra of the Cu 2p binding energy region obtained from catalysts: (a) fresh 5/5/90 CuO/ZnO/Al₂O₃, (b) spent 5/5/90 CuO/ZnO/Al₂O₃, (c) fresh 35/35/30 CuO/ZnO/Al₂O₃ catalyst, (d) spent 35/35/30 CuO/ZnO/Al₂O₃ catalyst, (e) fresh 42/47/11 CuO/ZnO/Al₂O₃ and (f) spent 42/47/11 CuO/ZnO/Al₂O₃. Dashed lines mark the peak positions of the Cu 2p peaks in the current paper and the dotted lines mark the CuO or Cu₂O plus Cu metal peak positions.

energy of 940–945 eV in the XPS spectra. The presence of the satellite peak is attributed to the interaction of the ejected photoelectron with another valence band electron, and/or to the metal-to-ligand charge transfer which has been demonstrated to occur in Cu^{2+} [29,45]. Satellite peaks are not present in Cu^0 or Cu^+ spectra due to the full 3d bands [30,45]. The presence of a Cu^{2+} species is in agreement with the XRD data, which indicates that CuO is the main Cu species before reduction and reaction. After charge corrections (see Section 2.8) the binding energy of the Cu 2p peaks on the fresh catalysts are centered at 933.6 eV, which is the reported binding energy for CuO [45–48]. However, the peaks are broad with significant shoulders at 935 eV. This high binding energy may indicate the presence of CuAl_2O_4 . The presence of this compound is further supported by the satellite-to-main peak intensity ratios (0.55–0.58), which are higher than that expected for CuO (0.45) although not as high as that expected for CuAl_2O_4 (1.1). Only catalyst 5/5/90 has a slightly larger ratio (0.65), which indicates that more CuAl_2O_4 is present on this catalyst compared to the 35/35/30 and the 42/47/11 catalysts. This would be expected due to the higher dispersion on this catalyst (a larger degree of Cu– Al_2O_3 interface and thus stronger Cu– Al_2O_3 interactions). However, the main Cu species on all the calcined catalysts is CuO, which agrees with the XRD data.

3.5.2. Spent catalysts

After reductive treatment and exposure to the reaction conditions, the Zn/Cu ratio increases on all catalysts (Table 4). This indicates that after reaction more ZnO covers the active Cu phase compared to before the reaction. This explains at least part of the catalyst deactivation since the active Cu surface area is reduced. In contrast, the C/Al ratio is relatively constant before and after reaction on all catalysts. The absence of carbon build-up at the surface suggests that coking is not a deactivation pathway on these catalysts. After exposure to the reaction conditions the binding energy of the Cu $2p_{3/2}$ peak is shifted to a lower value revealing reduction of the CuO. The peaks are also narrower after exposure to the reaction conditions as is expected from reduction of CuO to Cu_2O or Cu metal. The binding energies of the spent catalysts (after charge correction) are located at 932.4 eV, which is in agreement with Cu_2O and Cu metal [49]. However, the peaks are broader than what would be expected for pure Cu_2O or pure Cu metal, which again suggests that more than one Cu species are present on the surface. The absence of satellites in the spectra obtained from the spent catalysts indicates that no significant quantity of Cu^{2+} species is left on the surface. This supports our assignment of a ZnAl_2O_4 phase on the 35/35/30 catalyst, although it does not exclude presence of CuAl_2O_4 in the bulk of the catalyst.

Differentiating between the Cu^+ and Cu^0 valence states of copper compounds using the Cu 2p peaks is rather challenging due to the relatively large Cu radius and thus electronic binding energies are separated by only a small fraction of an eV [30,45–53]. Therefore, in order to determine the valence state of the Cu on the surface, the kinetic energy of the ejected Auger electrons was examined (Fig. 9) [48]. This energy does not depend on either the Cu $2p_{3/2}$ electronic binding energy or the energy of the incident radiation [50,53]. The Auger electron energy of Cu metal (918.6 eV) is higher than that of CuO (917.9 eV), while the Auger electron energy of Cu_2O is lower (916.7 eV). The signal to noise of the Auger electron energy region in the spectrum obtained from the fresh 5/5/90 catalyst is low and only a small feature at 916.2 eV can be observed (Fig. 9). Although this electron energy would suggest the presence of CuAl_2O_4 (electron energy 916.8 eV) rather than CuO (917.9 eV), it is known from the Cu 2p peaks that CuAl_2O_4 is not the major species on the surface. Consequently, the low electron energy observed could be due to charging. In contrast, both the

fresh 35/35/30 and 42/47/11 catalysts exhibit pronounced Auger features at 918.1 eV, which is the electron energy expected for CuO. After reduction and exposure to the reaction conditions, the Auger features shift to lower electron energies in all cases. This is indicative of Cu_2O formation rather than Cu metal formation. Consequently, the Cu metal on the reduced catalysts is oxidized to Cu_2O by steam during the reaction. However, the Auger peak is broad and the presence of Cu^0 in the near surface region cannot be excluded, but the dominant species at the surface is not Cu metal.

It is possible that both Cu metal and Cu_2O are required for an active catalyst and that the specific Cu^+/Cu^0 ratio determines the catalytic activity. For example, an oxygen-deficient surface is required for H_2O dissociation and formation of H_2 , while an oxidized surface is necessary for methanol dissociation and oxidation [31,54]. This could explain why the activities are not a simple function of the Cu metal surface areas. Furthermore, it is also known that CO binds strongly on Cu^+ , while it is adsorbed only weakly on metallic Cu [31]. Consequently, in the presence of Cu_2O the CO species will have time to react to CO_2 (assuming sufficient oxygen present on the surface), while on a more reduced Cu surface the CO is not bound as strongly and can desorb before reacting. It has in fact been observed that the CO concentrations increase with increasing extent of reduction on the surface of Cu-based methanol reforming catalysts [14]. The above could explain the trend in CO selectivity with temperature between 220 and 300 °C. The extent of Cu^0 oxidation to Cu^+ by the steam is likely to increase with the temperature in this range, which would be expected to increase the CO_2 over the CO product. At elevated temperatures the oxidation of Cu to Cu_2O by steam is negated by the reductive properties of methanol that is reacting over the catalyst. Consequently, at higher temperatures the surface is likely in a more reduced state (lower

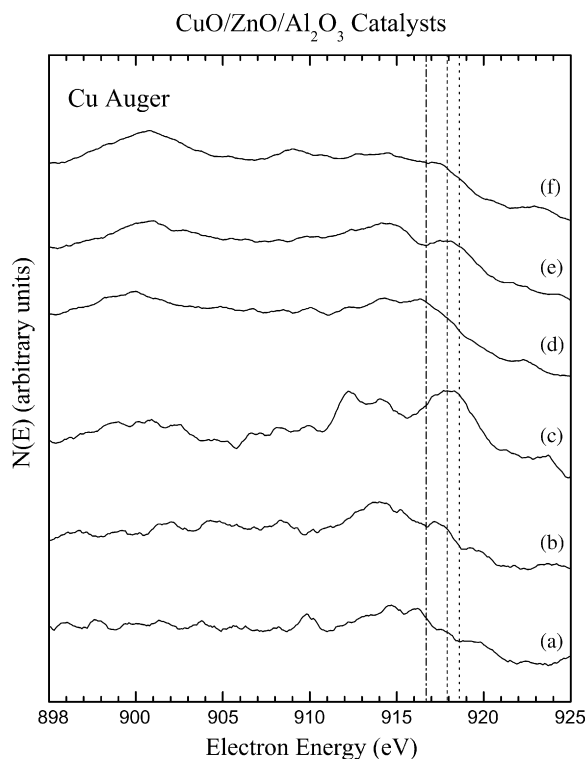


Fig. 9. XPS spectra of the Cu Auger kinetic energy region obtained from catalysts: (a) fresh 5/5/90 CuO/ZnO/ Al_2O_3 , (b) spent 5/5/90 CuO/ZnO/ Al_2O_3 , (c) fresh 35/35/30 CuO/ZnO/ Al_2O_3 catalyst, (d) spent 35/35/30 CuO/ZnO/ Al_2O_3 catalyst, (e) fresh 42/47/11 CuO/ZnO/ Al_2O_3 and (f) spent 42/47/11 CuO/ZnO/ Al_2O_3 . The dashed line marks the CuO peak position, the dotted line marks the Cu metal peak position and the dash-dotted line marks the Cu_2O peak position.

Cu^+/Cu^0 ratio) and the CO selectivity increases with temperature above 300 °C for all catalysts.

The Zn 2p, Al 2p and O 1s binding energy regions were also examined for all catalysts before and after reaction (not shown). However, these regions do not vary significantly between the catalysts and do not provide new information about the catalyst surface. For example, the Zn 2p peaks in ZnO and ZnAl_2O_4 are located at 1021.8 and 1021.7 eV, respectively and thus the XPS data alone cannot be used to differentiate between the two species [49]. The O 1s peaks are also not informative due to the presence of overlapping species. The O 1s peaks obtained from the 5/5/90 catalysts are dominated by the contribution from Al_2O_3 at 531.5 eV. The other catalysts 35/35/30 and 42/47/11 exhibit broad O 1s peaks due to Al_2O_3 , CuO at 529.8 eV, Cu_2O and ZnO at 530.5 eV and potentially also CuAl_2O_4 at 530.8 eV or ZnAl_2O_4 at 531.4 eV.

In summary, all nano-alumina-supported catalysts contain Cu_2O at the surface after exposure to the reaction conditions. While some Cu^+ likely is required for a high catalytic activity, it is possible that overoxidation, i.e. formation of CuO or bulk Cu_2O , decreases the catalytic activity. This could explain the lower activity observed for the 5/5/90 catalyst. However, the strong Cu– Al_2O_3 interactions on the 5/5/90 also appear to result in formation of more inactive CuAl_2O_4 , as well as a more difficult to reduce Cu_2O phase, compared to the other catalysts and may be the main reasons for the lower TOF observed for this catalyst.

3.6. Thermodynamic calculations

The results in this study reveal that for the nanoparticle-supported catalysts the CO selectivity does not increase with increasing temperatures between 220 and 300 °C. The fact that the CO selectivity is not increasing over this temperature range indicates that neither the reverse WGS nor the methanol decomposition reaction rate is increasing faster than the rate of the reforming reaction (CO production is not increasing faster than the CO_2 production rate). To elucidate the source of CO in this study, equilibrium calculations (reverse water-gas-shift reaction) were performed to compare the partial pressure of CO in the reactor effluent to the equilibrium partial pressure of CO for the reverse water-gas-shift reaction. The thermodynamic equilibrium constant for the reverse water-gas-shift was calculated according to Eq. (7):

$$K_{\text{eq}}^{\text{rWGS}} = \frac{p^{\text{CO}} \times p^{\text{H}_2\text{O}}}{p^{\text{CO}_2} \times p^{\text{H}_2}} = \exp(-\Delta G^{\text{rWGS}}/RT) \quad (7)$$

In this equation p^{CO} , p^{CO_2} , p^{H_2} , and $p^{\text{H}_2\text{O}}$ are the partial pressures of the components exiting the reactor. ΔG^{rWGS} is the free energy change associated with the reverse water-gas-shift reaction, R is the ideal gas constant and T is the temperature in Kelvins. In this way the exiting concentrations of the reaction products can be compared with the thermodynamic equilibrium of the reverse water-gas-shift. The results for the 35/35/30 catalyst are typical of the catalysts in this study and are shown in Fig. 10. Error bars indicate that even if there is 25% error in the measured gas pressures the conclusion that the CO concentrations are above levels which can be explained by the water-gas-shift equilibrium is still valid.

At all temperatures the partial pressure of CO in the reactor effluent is higher than the equilibrium CO partial pressure of the water-gas-shift reaction. Below 300 °C, the CO partial pressure approaches (decreases towards) the equilibrium value, but then sharply increases away from equilibrium above 300 °C. CO levels higher than those attainable via the water-gas-shift equilibrium indicate that the source of the CO is not solely the reverse water-gas-shift reaction. CO production at these levels must occur via the

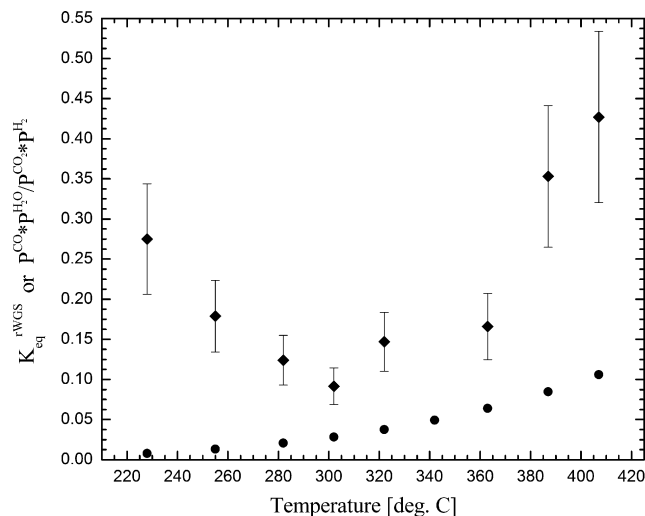


Fig. 10. Comparison of $K_{\text{eq}}^{\text{rWGS}}$ and ratio of measured partial pressures. (●) $K_{\text{eq}}^{\text{rWGS}}$ and (◆) $p^{\text{CO}} \cdot p^{\text{H}_2\text{O}} / (p^{\text{CO}_2} \cdot p^{\text{H}_2})$ over the 35/35/30 catalyst. Reaction conditions are the same as for Fig. 1.

decomposition reaction. This is reasonable particularly at higher temperatures given that the activation energy of the decomposition reaction is 170 kJ/mol [4] compared to 108 kJ/mol [12] for the reverse water-gas-shift. However, it appears that for the nanoparticle catalysts in this study, the decomposition reaction also must be taken into account at lower temperatures (and lower conversions) in agreement with the studies by Peppley et al. [4,17], Choi and Stenger [19] and Mastalir et al. [20].

4. Conclusions

The above results demonstrate that nanoparticle alumina can be used effectively as support in the preparation of highly active Cu–ZnO steam reforming catalysts. Very high copper surface areas can be attained on nanoparticle alumina and activities similar to those of commercial catalysts with much high copper contents can also be achieved. However, the activities of the catalysts do not scale with the copper surface area and high Al_2O_3 concentrations tend to retard the surface activity. Strong metal–support interactions between the small copper particles and the nanoparticle Al_2O_3 support on catalysts with high Cu dispersions, such as the 5/5/90 catalyst, appear to have a dramatic influence on the redox properties of the catalyst. The change in redox properties likewise appears to affect the methanol conversion, with less reducible nanoparticle catalysts having lower conversions. High Al_2O_3 concentrations also promote production of an undesired formaldehyde byproduct.

The results in this study demonstrate that novel catalysts prepared using nanoparticle alumina have the advantage of lower CO selectivities compared to a commercially available low temperature shift catalyst. In fact, below reaction temperatures of 300 °C (260 °C for the 42/47/11 catalyst) the CO selectivity over the nanoparticle catalysts decreases with increasing temperature. This is unexpected and observed only for the nanoparticle-based catalysts, and must thus be due to changes in the surface composition of the nanoparticle systems, such as the Cu^+ to Cu^0 ratio, over this temperature range. It was also shown that use of a nanoparticle support results in a more active copper surface (evidenced by higher turnover frequencies) compared to a commercially available reference catalyst.

XRD reveals that Cu metal is present in the bulk of all the spent catalysts and XPS indicate that Cu_2O and perhaps a small amount

of CuAl_2O_4 are present at the surface. Only on the 5/5/90 could the Cu_2O phase be detected with XRD. There is also evidence of a ZnAl_2O_4 spinel phase in the bulk of the 35/35/30 catalyst. The high stability of the 35/35/30 catalyst is likely due to a beneficial interaction between the zinc-aluminate species and the Cu species on the catalyst. Although it could also be due to the fact that there is less ZnO available that can migrate and cover the active Cu phase.

The CO production levels are above what can be explained from the water-gas-shift equilibrium for the nanoparticle catalysts at all temperatures. This indicates that the methanol decomposition reaction is partly responsible for CO production. The results in this study suggest that it is the nature of the interaction between the copper and promoter or support, and not simply the copper surface area, which determines the catalytic activity.

Permanent catalyst deactivation is likely due to ZnO covering part of the active Cu phase, although loss of activity, and increasing CO selectivities, at higher temperature may also be due to decreasing Cu^+/Cu^0 ratios.

Acknowledgements

This work was supported by NASA Glenn Research Center, Grant NAG 3-2930, monitored by Mr. Tim Smith. Partial financial support was also obtained from DOE.

XRD and XPS measurements were performed at the Major Analytical Instrumentation Center at the University of Florida. The authors are especially thankful for the advice and instruction of Dr. Eric Lambers and Dr. Valentin Craciun.

The BET data were collected at the Particle Engineering Research Center at the University of Florida. The authors are grateful for the training on the machine provided by Mr. Gill Brubaker.

We also thank Dr. Gar Hoflund for letting us use his XPS system and Dr. Michael Everett for technical assistance with the XPS measurements.

References

- [1] B. Lindström, L.J. Peterson, *Int. J. Hydrogen Energy* 26 (2001) 923–933.
- [2] J. Leddy, J. Fenton, *Electrochem. Soc. Interface* (2005) 21–23.
- [3] N.E. Vanderborgh, B.E. Goodby, T.E. Springer, *Proc. 32nd Int. Power Sources Symp.* (1986) 623–628.
- [4] B. Peppley, J.C. Amphlett, L.M. Kearns, R.F. Mann, *Appl. Catal. A* 179 (1999) 21–29.
- [5] V. Agarwal, S. Patel, K.K. Pant, *Appl. Catal. A* 279 (2005) 155–164.
- [6] B.L. Knip, T. Ressler, A. Rabis, F. Girgsdies, M. Baenitz, F. Steglich, R. Schlögl, *Angew. Chem. Int. Ed.* 43 (2004) 112–115.
- [7] J. Agrell, H. Birgersson, M. Boutonnet, I. Melian-Cabrera, R.M. Navarro, J.L.G. Fierro, *J. Catal.* 219 (2003) 389–403.
- [8] G. Moretti, G. Ferraris, G. Fierro, M. Lo Jacono, *Surf. Interface Anal.* 38 (2006) 224–228.
- [9] P.H. Matter, D.J. Braden, U.S. Ozkan, *J. Catal.* 223 (2004) 340–351.
- [10] R. Figueiredo, A. Martinez-Arias, M. Granados, J.L. Fierro, *J. Catal.* 178 (1998) 146–152.
- [11] J. Agrell, H. Birgersson, M. Boutonnet, *J. Power Sources* 106 (2002) 249–257.
- [12] H. Purnama, T. Ressler, R.E. Jentoft, H. Soerijanto, R. Schlögl, R. Schomacker, *Appl. Catal. A* 259 (2004) 83–94.
- [13] M. Turco, G. Bagnasco, U. Costantino, F. Marmottini, T. Montanari, G. Ramis, G. Busca, *J. Catal.* 228 (2004) 56–65.
- [14] P. Pfeifer, K. Schubert, G. Emig, *Appl. Catal. A* 286 (2005) 175–185.
- [15] J. Agrell, K. Hasselbo, K. Jannson, S. Jaras, M. Boutonnet, *Appl. Catal. A* 211 (2001) 239–250.
- [16] R.J. Burch, S.E. Golunski, M.S. Spencer, *Catal. Lett.* 5 (1990) 55–60.
- [17] B.A. Peppley, J.C. Amphlett, L.M. Kearns, R.F. Mann, *Appl. Catal. A* 179 (1999) 31–49.
- [18] J. Amphlett, M. Evans, R. Jones, R. Mann, R. Weir, *Can. J. Chem. Eng.* 59 (1981) 720–727.
- [19] Y. Choi, H. Stenger, *Appl. Catal. B* 38 (2002) 259–269.
- [20] A. Mastalir, B. Frank, H. Soerijanto, A. Deshpande, M. Niederberger, R. Schomacker, R. Schlögl, T. Ressler, *J. Catal.* 230 (2005) 464–475.
- [21] S. Murcia-Mascarós, R. Navarro, L. Gómez-Sainero, U. Constantino, M. Nocchetti, J.L. Fierro, *J. Catal.* 198 (2001) 338–347.
- [22] C.J. Jiang, D.L. Trimm, M.S. Wainwright, *Appl. Catal. A* 93 (1993) 245–255.
- [23] A. Szizyalski, F. Girgsdies, A. Rabis, Y. Wang, M. Niederberger, T. Ressler, *J. Catal.* 233 (2005) 297–307.
- [24] H. Oguchi, H. Kanai, K. Utani, Y. Matsumura, S. Imamura, *Appl. Catal. A* 293 (2005) 64–70.
- [25] H. Purnama, F. Girgsdies, T. Ressler, J.H. Schattka, R.A. Caruso, R. Schomacker, R. Schlögl, *Catal. Lett.* 94 (2004) 61–68.
- [26] T.L. Reitz, P.L. Lee, K.F. Czaplewski, J.C. Lang, K.E. Popp, H.H. Kung, *J. Catal.* 199 (2001) 193–201.
- [27] A. Sepulveda, C. Marquez, I. Rodriguez-Ramos, A. Guerrero-Ruiz, J.L. Fierro, *Surf. Interface Anal.* 20 (1993) 1067–1074.
- [28] L. Yong-Feng, D. Xin-Fa, L. Wei-Ming, *Int. J. Hydrogen Energy* 29 (2004) 1617–1621.
- [29] M.N. Barroso, M.F. Gomez, J.A. Gambo, L.A. Arrúa, M.C. Abello, *J. Phys. Chem. Solids* 67 (2006) 1583–1589.
- [30] B. Strohmeier, D. Leyden, R. Field, D. Hercules, *J. Catal.* 94 (1985) 514–530.
- [31] M. Turco, G. Bagnasco, U. Costantino, F. Marmottini, T. Montanari, G. Ramis, G. Busca, *J. Catal.* 228 (2004) 43–55.
- [32] T. Takeguchi, Y. Kani, M. Inoue, K. Eguchi, *Catal. Lett.* 83 (2002) 49–53.
- [33] G.C. Chinchin, C.M. Hay, H.D. Vandervell, K.C. Waugh, *J. Catal.* 103 (1987) 79–86.
- [34] J.P. Breen, F.C. Meunier, J.R.H. Ross, *Chem. Commun.* (1999) 2247–2248.
- [35] H.A.E. Hagelin, J.F. Weaver, G.B. Hoflund, G.N. Salaita, *J. Electron Spectrosc. Rel. Phenom.* 124 (2002) 1–14.
- [36] W. Dai, Y. Cao, L. Ren, X. Yang, J. Xu, H. Li, H. He, K. Fan, *J. Catal.* 228 (2004) 80–91.
- [37] M.M. Günter, T. Ressler, R.E. Jentoft, B. Bems, *J. Catal.* 203 (2001) 133–149.
- [38] E. Lambert, Mineralogical-Petrograph Institute, Universität Heidelberg, Germany, ICDD Grant-in-Aid (1980).
- [39] F. Swanson, *Natl. Bur. Stand. (U.S.) Circ.* 539 (2) (1953) 38.
- [40] M. Kalliomaki, V. Meisalo, A. Laisaar, *Phys. Status Solidi* 56 (1979) K127–K131.
- [41] H. Oguchi, T. Nishiguchi, T. Matsumoto, H. Kanai, K. Utani, Y. Matsumura, S. Imamura, *Appl. Catal. A* 281 (2005) 69–73.
- [42] J. Klein, C. Li, D. Hercules, J. Black, *Appl. Spectrosc.* 38 (1984) 729–733.
- [43] J. Pike, S. Chan, F. Zhang, X. Wang, J. Hanson, *Appl. Catal. A* 303 (2006) 273–277.
- [44] J.P. Breen, J.R.H. Ross, *Catal. Today* 51 (1999) 521–533.
- [45] N. McIntyre, T. Rummery, M. Cook, D. Owen, *J. Electrochem. Soc.* 123 (1976) 1164–1170.
- [46] N. McIntyre, M. Cook, *Anal. Chem.* 47 (1975) 2208–2213.
- [47] J. Ghijsen, L. Tjeng, J. van Elp, H. Eskes, J. Westerlink, G. Sawatzky, M. Czyzyk, *Phys. Rev. Lett.* B 38 (1988) 11322–11330.
- [48] C. Chusuei, M. Brookshier, D. Goodman, *Langmuir* 15 (1999) 2806–2808.
- [49] C.D. Wagner, A.V. Naumkin, A. Kraut-Vass, J.W. Allison, C.J. Powell, J.R. Rumble Jr., NIST Standard Reference Database 20, Version 3.4 (Web Version), <http://srdata.nist.gov/xps/>.
- [50] T. Carlson, *Photoelectron and Auger Spectroscopy*, Plenum Press, New York, NY, 1975.
- [51] G. Schön, *Surf. Sci.* 35 (1973) 96–107.
- [52] G. Schön, *J. Electron Spectrosc. Relat. Phenom.* 1 (1972) 377–387.
- [53] C. Brundel, C. Evans, S. Wilson, *Encyclopedia of Materials Characterization*, Butterworth-Heinemann Publishing, Stoneham, MA, 1992.
- [54] T.H. Ellis, H. Wang, *Langmuir* 10 (1994) 4083–4088.